Chapter 4

Characteristics of RSG simulations

Contents

In this Chapter, I study the characteristics of our RSG simulations. For this purpose I have used my code OPTIM3D and some other routines in IDL (the language used by Freytag and collaborators to handle the output of CO^{5}BOLD).

Before presenting the properties of the the numerical simulations, it is necessary to introduce the contribution function to the line depression. This quantity will be used to average the velocity field in order to show the contribution from different parts of the stellar surface to the Doppler shifts at one wavelength.

4.1   Contribution functions

The knowledge of the average depth of formation of spectral lines is essential for the study of depth-dependent phenomena in stellar atmospheres. The depth of formation of spectral lines is generally estimated through the *contribution function* (CF).
A first definition of CF, is the contribution function to the specific intensity. It derives

from the solution of the radiative transfer equation for the emerging intensity (here for the direction towards the observer)

$$I(0) = \int_0^\infty S e^{-\tau} d\tau \tag{4.1}$$

The integrand of equation 4.1 represents the fraction of the emergent intensity originating from depth τ and is referred to the CF to the emerging intensity.
This expression cannot be used to determine the depth of the layers of formation of a spectral line because there is a difference between the contribution function of the emergent intensity and the contribution function of the *line depression*. Magain (1986) gives an example: the CF derived from Eq. 4.1 would place the line formation layers of a telluric water vapor line superimposed on the solar spectrum in the solar atmosphere rather than in the Earth's. Even if the the absorption happens in the Earth atmosphere, the photons of the residual intensity come from the solar atmosphere.
To overcome the problem, Magain (1986) proposed the contribution function of the relative intensity depression R

$$R(0, \lambda) = \frac{I_c(0, \lambda) - I_l(0, \lambda)}{I_c(0, \lambda)} \tag{4.2}$$

where c stands for continuum and l for line.
He considered the transfer equation for R

$$\frac{dR}{dz} = k_R (R - S_R) \tag{4.3}$$

with the formal solution

$$R(0, \lambda) = \int_0^\infty S_R e^{-\tau_R} d\tau \tag{4.4}$$

where the "effective absorption coefficient" k_R is

$$k_R = k_l + k_c \frac{S_c}{I_c} \tag{4.5}$$

and the "effective source function" S_R is

$$S_R = \left(1 - \frac{S_l}{I_c}\right) / \left(1 + \frac{k_c}{k_l} \frac{S_c}{I_c}\right) \tag{4.6}$$

and $d\tau_R = k_R \rho dz$. The CF to the line depression may be written (in the log τ_0 scale), writing $x = \lg(\tau_0)$, as

$$CF_R(x) = (\ln 10) \tau_0 \frac{k_l}{k_0} \left(1 - \frac{S_l}{I_c}\right) e^{-\tau_R} \tag{4.7}$$

where k_0 is a reference opacity (e.g., k_{Ross} or k_{5000}).
The CF_R is non-zero in a layer only if: (i) $k_l \neq 0$; that implies the presence of absorbers in the layer, (ii) $S_l \neq I_c$; so that the re-emitted light must not be equal to the absorbed

light, the line will appear in absorption if $S_l < I_c$ and in emission if $S_l > I_c$.

Except for the Sun, it is not possible to resolve the stellar disk intensity and for all other stars, the observed line profile therefore consists of contributions from different angles. Albrow & Cottrell (1996) proposed a different approach based of the absolute flux depression ($Q(\tau) = I_c - I_l$) in the surface intensity ($Q(\tau = 0)$). They solve the transfer equation for Q and they found the formal solution for the absolute depression in the surface intensity

$$Q(0,\lambda) = \int_0^\infty S_Q e^{-\tau} d\tau \tag{4.8}$$

where

$$S_Q = \frac{k_l}{k_l + k_c}(I_c - S_l) \tag{4.9}$$

and the contribution function as

$$CF_Q(\tau) = \frac{k_l}{k_c + k_l}(I_c - S_l)e^{-\tau} \tag{4.10}$$

and in the $\lg(\tau)$ scale

$$CF_Q(x) = (\ln 10)\,\tau_0\frac{k_l}{k_0}(I_c - S_l)e^{-\tau} \tag{4.11}$$

I have use the Eq. 4.11 for computing the contribution functions.

Following Magain, I define also the average depth of formation of line depression at a given wavelength λ

$$<x>(\lambda) \equiv \frac{\int_{-\infty}^{+\infty} x CF_Q dx}{\int_{-\infty}^{+\infty} CF_Q dx} \tag{4.12}$$

In a similar way, I computed the mean of other quantities such as the velocity, temperature, density, etc. This is valid only if CF_Q does not change sign, which is generally true in the case of absorption lines.

4.2   Fundamental parameters definitions

In this Section I define how I calculate the fundamental parameters of the models.

The radius is difficult to define in RSGs because they have an extended atmosphere, as a consequence also the effective temperature and surface gravity are not well defined. A reasonable and frequent definition of the radius is linked to the Rosseland optical depth scale: the stellar radius is the radius at $\tau_{\mathrm{Rosseland}} = 1$.

For RHD simulations I have followed a different approach using the existing routines by Dr. Freytag. First, I have collected the average luminosity over spherical shells (L_{radius}) for each snapshot of a simulation. It is important to separate each snapshot because the

luminosity (and also the other variables) varies with time. Then, I have defined the stellar radius, $R_\star$, as the radius where the local temperature is equal to the effective temperature

$$L_{\mathrm{radius}}/\left(4\pi R^2\right) = \sigma T^4 \tag{4.13}$$

where R is the stellar radius, the temperature is T and σ is the Stefan-Boltzmann constant.

B. Plez has tested the method described in Eq. 4.13 with the MARCS code (Plez et al. 1992 and Gustafsson et al. 2008). In MARCS code, the stellar radius is defined as the radius where $\tau_{\mathrm{Rosseland}} = 1$. Using the definition 4.13 on different MARCS models, the difference between this method and the MARCS definition is lower than 1%. Also the effective temperature has the same difference, lower than 1%.

The effective temperature is derived from the radius computed from 4.13

$$T_{\mathrm{eff}} = \frac{L_{\mathrm{out}}}{4\pi R_\star^2 \sigma} \tag{4.14}$$

where L_{out} is the emerging luminosity in the upper layers of the simulation.

and the surface gravity

$$g = 4\pi G \frac{M}{R_\star^2} \tag{4.15}$$

where G is the gravitation constant and M is the stellar mass.

The average over spherical shells used for collecting the important variables is an approximation and the reader must remember that the fluctuations of the average variables can be really intense (see Sect. 4.4). However, this procedure allows a quantitative determination of the fundamental parameters.
An important point is that the luminosity varies with time and this influences the stellar radius, the effective temperature and the surface gravity. In Tab. 4.1 I report the fundamental parameters of the simulation used in this work. The Table shows their average over time, and the one sigma fluctuations with respect to the average over time.

4.3 Are the RSG simulations relaxed?

I can say that a simulation is relaxed when the fluctuations of the radius, luminosity, effective temperature are constant with respect to the time. However, in RHD simulation there are always small changes going on, even if a large number of runs have been computed. The typical picture of RHD simulations is presented in Fig. 4.1 for simulation st35gm03n07 and Fig. 4.2 for simulation st35gm03n05 (Tab. 4.1). The first model has a lower resolution (235^3 grid points) than the second one (315^3 grid points). st35gm03n07 is believed to be relaxed because it has a large number of runs and the fluctuations in luminosity ($\sim 2\%$), temperature ($\sim 0.4\%$) and radius ($\sim 0.2\%$) are small. The high resolution model runs needs more computational time to be relaxed and this explains the fact

that the stellar time of st35gm03n07 is 60% larger than st35gm03n05. As a consequence, st35gm03n05 has larger luminosity ($\sim 5\%$), temperature ($\sim 1.3\%$) and radius ($\sim 0.5\%$) fluctuations than the previous one but I can consider it relaxed also.

In both cases, it is visible a drifting of the parameters especially for the radius. Simulation st35gm03n07 in Fig. 4.1 is one of the most used in this work. The total amount of computational time is 7.5 years, however, I have considered only the last 3.5 years (i.e., what is displayed in the Figure). In bottom right panel, I have fitted the radius with a polynomial fit that shows the stabilization of the drifting radius over the last year. It would be interesting to see what happens afterwards but, considering the large CPU time needed, this is the actual state-of-the-art of the RHD simulation used in this work. In conclusion, one simulation can be considered relaxed when the stellar parameters do not drift with time.
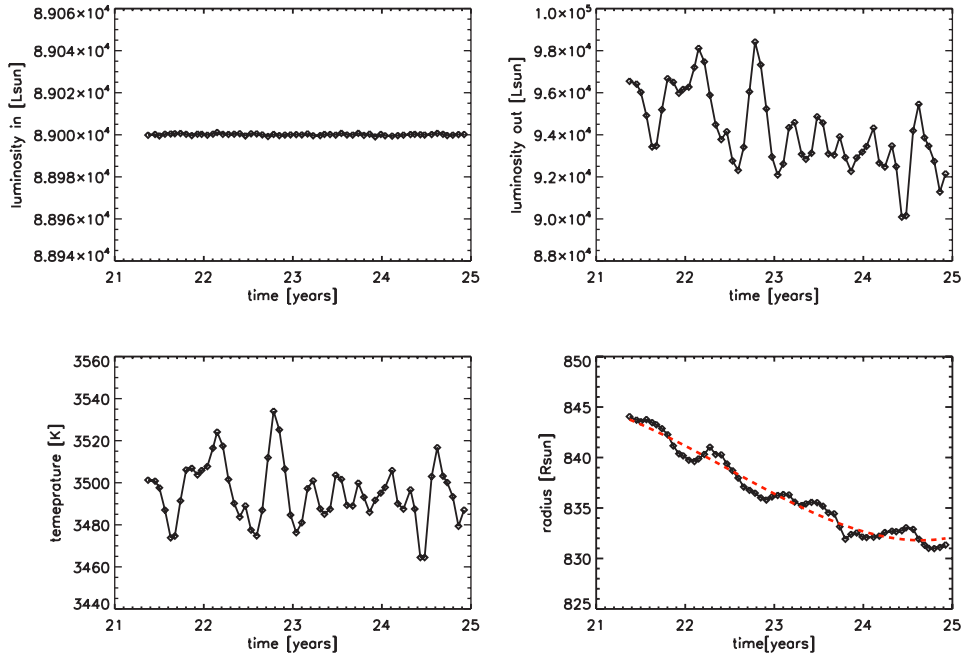

Figure 4.1: Input luminosity, outgoing luminosity, temperature and radius for a temporal series of model st35gm03n07 (235^3 grid points simulation, see Tab. 4.1). The red dashed line is a polynomial fit of degree 5.

From the Figures, it is evident that the input luminosity (upper left panel, see Sect. 2.3) is not equal to the outgoing luminosity (upper right panel). This is due to the fact that the input luminosity is the luminosity per core volume. It might be that there is a shortcoming/bug (B. Freytag, private communication) in the computation of the core volume because it is not exactly spherical but made of very small cubes. However, the outgoing luminosity tends to decrease and this affect the radius. Even at this quite long running stage of the simulation, something is still happening in the core. In Fig. 4.3 it is visible that nearby the last time-steps, the temperature increases and this could affect the luminosity and the radius. The reason is not clear and further investigations should
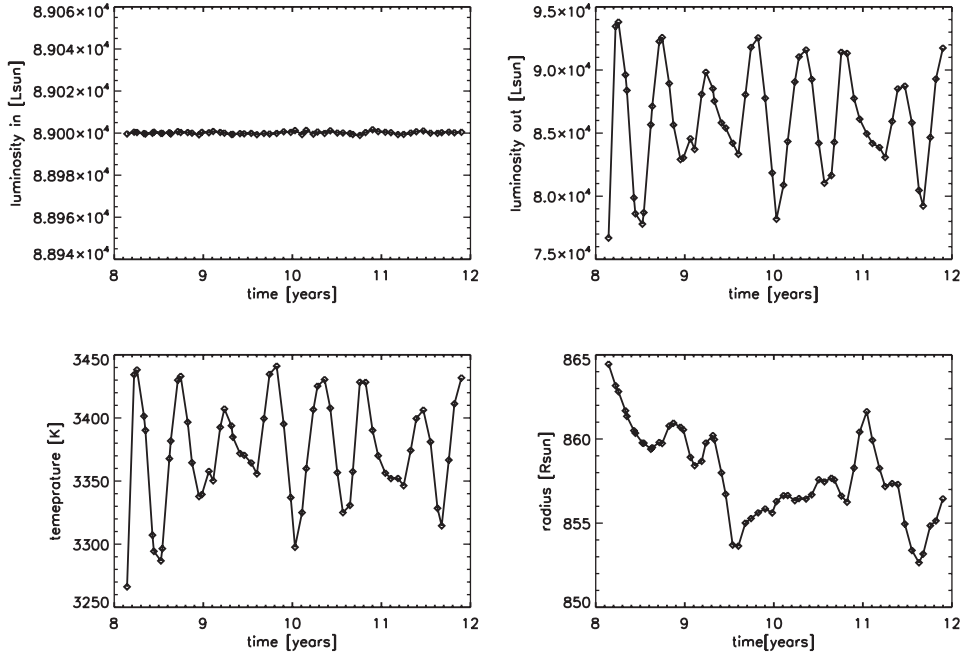
Figure 4.2: Input luminosity, outgoing luminosity, temperature and radius for a temporal series of model st35gm03n05 (315^3 grid points simulation, see Tab. 4.1).

be done simply running for much more stellar-time one simulations and monitoring the luminosity and radius tendency.

A special case is the model st35gm03n04. It presents very low luminosity ($\sim 3.3\%$), temperature ($\sim 0.8\%$) and radius ($\sim 0.4\%$) fluctuations and a long period is covered (6.8 years). The simulation should be considered relaxed. Contrary to the other models, the radius is getting larger with respect to the time. This can be due to the fact that the lower effective temperature with respect to the other simulations causes a more extended atmosphere. Or st35gm03n04 may not be completely relaxed even if the fluctuations are small and the last phases of the calculated simulation are characterized by an atmospheric expansion.

High (315^3) and medium-high (235^3) resolution (except for st35gm03n04) show the same behavior concerning the fundamental parameters of the RHD simulations.

Another point of concern is the Cartesian grid. The influence of the cubical box and the Cartesian grid is strongest in the phase of the initial onset of convection. At later stages, there is no alignment of structures with the grid nor any tendency for the shape of the star to become cubic.
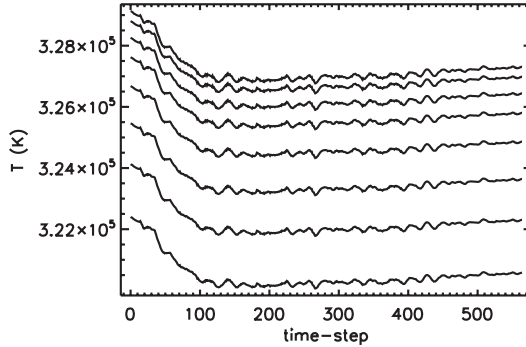
Figure 4.3: Temporal evolution of the average over spherical shells of the temperature of the innermost grid points of the model st35gm03n07: from the top the very center point of the cube. The temperature goes up to ~ 300000K as shown in Fig. 2.10, top left panel.

4.4 Average temperature and density profile

In this Section, I analyze the temperature and density profiles of one snapshot of the RHD simulation st35gm03n07 (Tab. 4.1). Fig. 4.4 displays the average temperature (left panel) and density (right panel) over spherical shells compared to two MARCS models at 3200K and 3600K.
It is not straightforward to compute the optical depth scale for different angles in the computational cube (with OPTIM3D I compute the optical depth on the line-of-sight). In fact, it is more precise to average the temperature and density of the inclined rays. Instead, I computed an average over spherical shells of the temperature and density. Anyway, these averages give an idea of the behavior of these quantities. The largest fluctuations at one sigma with respect to the average value occurs at $\tau = 1$ and they are about 60% (both for density and temperature).

The three-dimensional temperature profile (black line) has a gradient larger than 0 (typical of the plan parallel grey model, dashed line) and also larger than the gradient resulting from a spherical grey model[13]. Thus, even if the radiation transfer uses a grey-approximation in the RHD models, the outer layers cool down thanks to the convective overshoots that are strongly influenced by the temperature structure of the atmosphere. In fact, the gas motions overshooting from the convective envelope into the stably stratified layers of a stellar atmosphere try to establish a temperature profile close to adiabatic. On the other hand, radiation tries to keep the thermal structure close to radiative equilibrium conditions. The temperature results from the balance between the two controlling processes (see e.g., Stein & Nordlund 1998 and Ludwig et al. 1994).
The one-dimensional models appear cooler in the outer atmosphere ($\log(\tau)$<-2) than the three dimensional one. This is a consequence of the more detailed line blanketing calculation. Around $\log(\tau)$=0, the average three-dimensional temperature is much hotter

---

[13]If the grey model is spherical, the resulting temperature at $\log(\tau)$<-6 would be $\sim 4\%$ smaller (Gustafsson et al. 2008). In this case the temperature would be 2738K instead of 2850K and the gradient is not equal to zero.
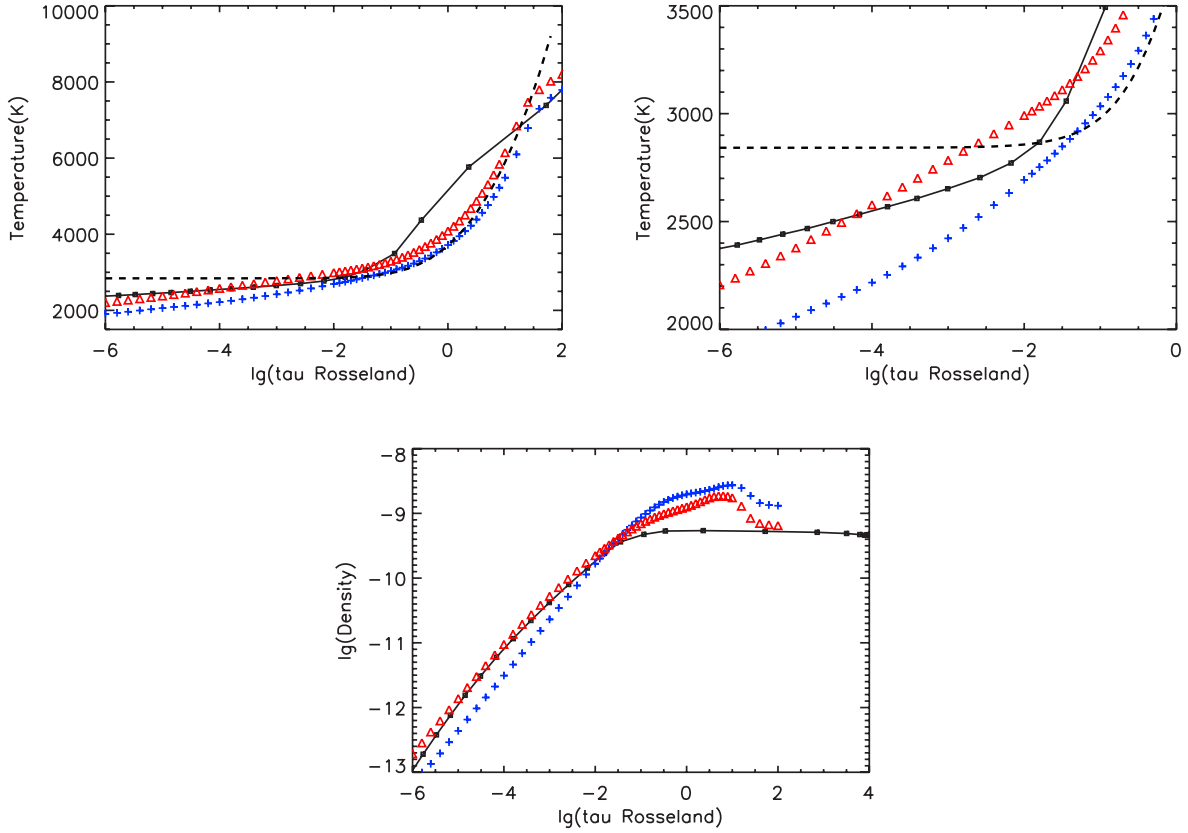
Figure 4.4: *Top left panel:* average temperature (black curve) over spherical shells for one snapshot of the simulation st35gm03n07 (Tab. 4.1). The model's resolution is indicated with the black points. The dashed line corresponds to a grey plan parallel model at 3500 K. *Top right panel:* Enlargement of the average temperature profile. *Bottom panel:* average density over spherical shells for one snapshot of the simulation st35gm03n07.
The average quantities are compared to MARCS models at T_{eff}=3200K (blue line) and 3600K (red line), log(g)=-0.5, microturbulence=2km/s, solar metallicity.

than in MARCS models, however, the temperature fluctuations are large and the one-dimensional temperature profile and there may be ray with a temperature close to the MARCS model. In the deeper layers (log(τ>1.5), the convective flux prevails and the three-dimensional temperature is cooler with respect to the one-dimensional models and grey models profiles.

The three-dimensional density profile behaves like MARCS models in the outer atmosphere, while at log(τ)=0 the density fluctuations contains again the one-dimensional density profile. The density-inversion noticeable for MARCS models at log(τ)=2 is due to the turbulent pressure term that is considered. With this recipe, the one-dimensional models profile is really similar to the three-dimensional one (at this depth the fluctuations of the three-dimensional models are much smaller that at log(τ)=0). It would be interesting to compute a MARCS model farther deep in order to see if the general trend of the density and temperature profiles stay close the three-dimensional ones.

4.5 Numerical resolution

Numerical resolution is CPU-time demanding. Current resolutions span values from 95^3 to 315^3 grid points. The available number of points per convective elements is smaller for a higher mass (current higher mass is 12 $M_\odot$) star and the resolution of the surface layers is not very good.
There are not so many RHD simulations available and it is difficult to compare models with different resolution because also the fundamental parameters vary at the same time. Simulations at 235^3 grid points constitute the largest sample of $12M_\odot$ models. The numerical resolution of 235^3 grid points is then the best I have for this work (also in term of relaxed model). I found that this resolution constitutes a good description of the surface structures that affect interferometric visibilities. Increasing the resolution (from 127^3 to 235^3 grid points) small structures appear within the large granules (see Sect. 8.4.1). These small structures have a typical dimension of 40- 50 $R_\odot$ (5% of the stellar radius) and they affect the visibility curves up to the fourth-fifth lobe.
Furthermore, the preliminarily results (Sect. 5.2) show also that the velocity field seems not to change when passing from 235^3 to 315^3 grid points model.

Concerning the spectral synthesis, the flux fluctuations at one sigma with respect to the average value are $\sim 15\%$ for 235^3 grid points model and $\sim 20\%$ for the 127^3 (the temporal average has been done over $\sim$230 days, Fig. 4.5).
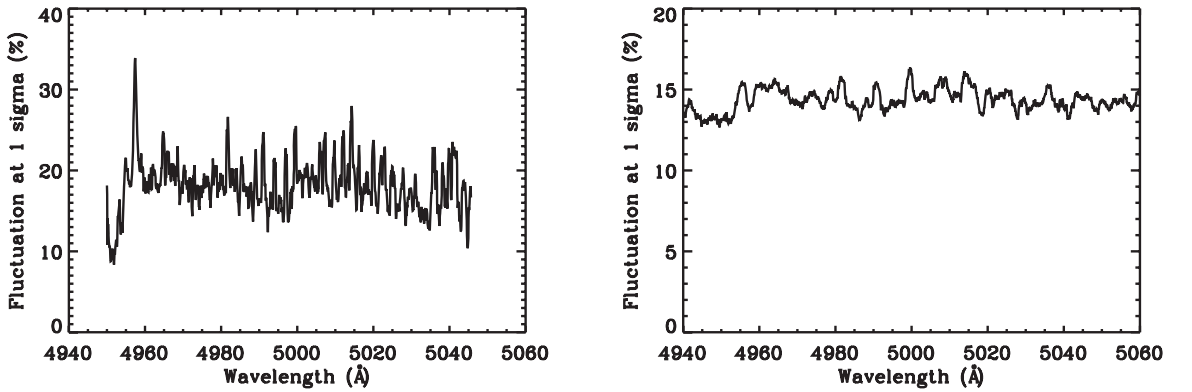

Figure 4.5: Fluctuations of the flux at one sigma with respect to the average flux. The time covered is about 230 days. *Left panel:* simulation st35gm04n30 (Tab. 4.1) at 127^3 grid points. *Right panel:* simulation st35gm03n07 at 235^3 grid points.

If the resolution of 127^3 is enough to resolve all the structures and variations there would not be a difference between the fluctuations of resolution 127^3 and 235^3. However, the ratio between the fluctuations F, from Fig. 4.5, is not 1:

$$\frac{F_{235}}{F_{127}} = \frac{15\%}{20\%} = 0.75 \qquad (4.16)$$

Therefore, with resolution 235^3 the structures are resolved better than for resolution

127^3.

In addition, the numerical resolution influences the spectral synthesis because the sampling in the region where the spectrum forms is poor. Fig. 4.6 displays the contribution function (CF) to the spectral line flux depression (see Sect. 4.1 for some areas on the stellar surface at the pseudo-continuum wavelength of 5236.88 Å (the model used is st35gm03n05 in Tab. 4.1). As expected, the continuum CF peaks at $\tau=1$. In the outer layers (for $\log(\tau)$ lower than -1, i.e. where the contribution of the lines is important) the sampling is rather good, while in the region where the continuum forms there are fewer points in the tau scale.
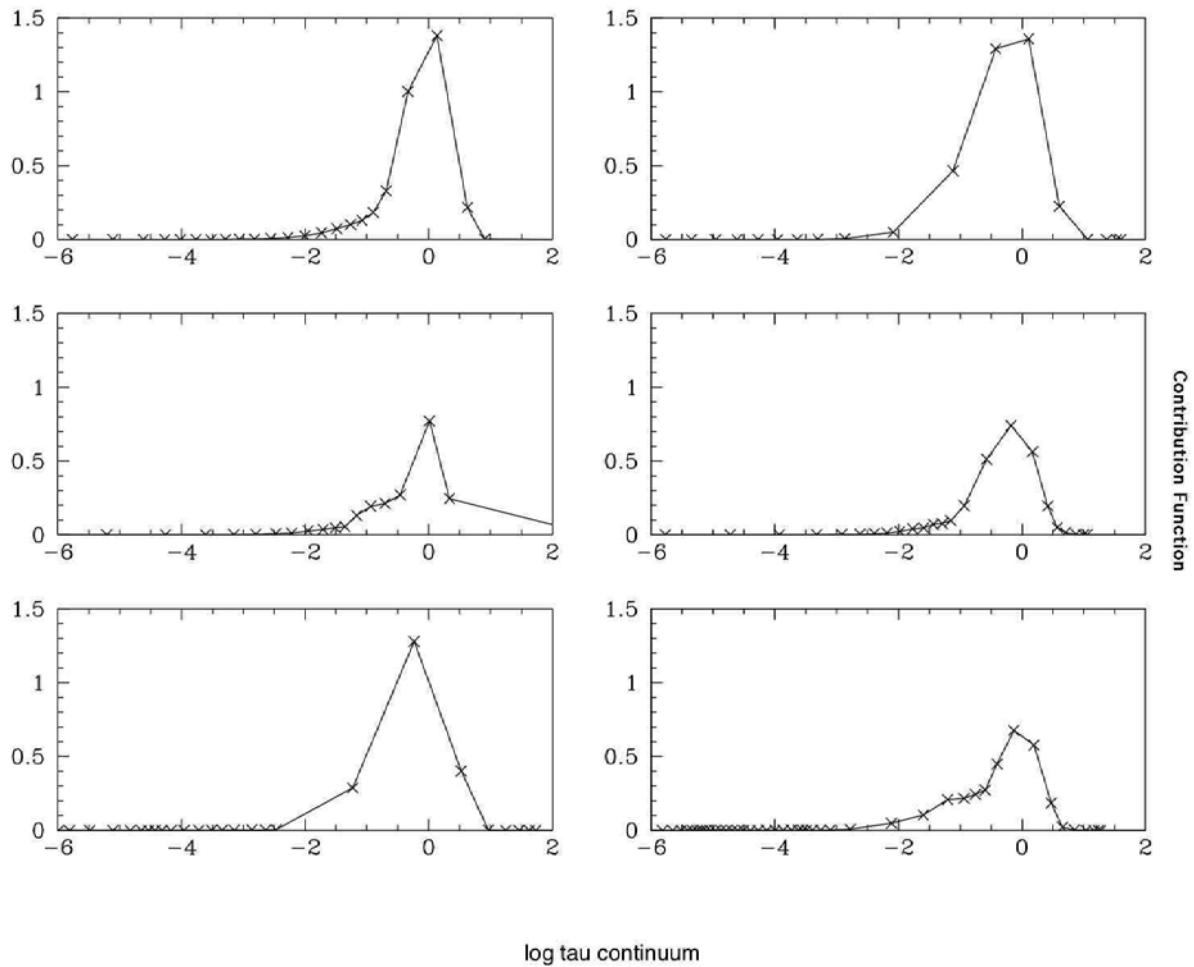

Figure 4.6: Impact of a high resolution RHD model (315^3 grid points) resolution on the contribution function at 5236.88 Å. The six panels represent different locations on the stellar surface.

4.6 The simulations used in this work

The table presented in this Section reports the principal simulations I have used for post processing analysis.

All the simulations present fluctuations variable with time for their fundamental parameters, even if they are small for long runs. In general, the high resolution (315^3 grid points) models have less runs because of their high CPU-time demanding (see Sect. 2.3.4).

In this work, I have mostly used the simulation st35gm03n07 for the interferometric and spectroscopic analysis because this model is the closest available to the Betelgeuse effective temperature (3650K, Levesque et al. 2005) and it has the largest number of runs (see Sect. 4.3). st35gm03n06 could have also been chosen because it is also relaxed and covers many stellar years. However, the effective temperature is lower than the observed one.

The highest resolution models have been used only occasionally because of their small temporal extension.

New models are on-going with the aim to increase the surface gravity and the effective temperature with a 235^3 grid points resolution in order to have a large coverage of the HR diagram.

Table 4.1: CO^{5}BOLD simulations used in this work, all these models are fully relaxed or stopped. Basic model parameters: the original model name (made from the first two digits of the approximave effective temperature, the approximave surface gravity, and a running number), the number of grid points, the physical size of the computational box, the mass used to compute the gravitational potential and the envelope mass, the time covered by the simulation, the average over time of the luminosity, effective temperature, radius and surface gravity, the errors are the one sigma fluctuations with respect to the average over time; comment.

Model Name	Resolution (grid points)	Box ($R_\odot$)	Mass ($M_\odot$)	Period coverd (years)	Luminosity ($L_\odot$)	T_{eff} (K)	Radius ($R_\odot$)	log g	Comment
st35gm04n30	127³	1669	5	12.6	40792.0[a]±4562.8	3140.0[a]±102. 0	681.0[a]±8.7	-0.53[a]	
st35gm04n29	235³	1669	5	7.4	41145.8[b]±1597.2	3265.7[b]±35.3	633.3[b]±5.1	-0.47[b]	
st35gm03n04	235³	2081	12	6.9	83512.8[c]±2802.7	3335.4[c]±27.1	864.8[c]±3.0	-0.37[c]	Not relaxed?
st35gm03n05	315³	2081	12	2.8	86013.7±4364.2	3373.1±43.2	858.0±2.6	-0.37	
st35gm03n06	235³	2081	12	17.8	94623.9[d]±2108.3	3436.0[d]±18.6	867.6[d]±5.5	-0.34[d]	
st35gm03n07	235³	2081	12	7.5	94189.0[e]±1871.5	3495.2[e]±14.3	836.5[e]±4.1	-0.34[e]	Best model so far
st35gm03n08	315³	2081	12	0.7	99216.0±1871.5	3445.2±36.4	883.5±4.3	-0.39	Model stopped prematurely

[a]average over last 2.5 years
[b]average over last 3.1 years
[c]average over last 2.2 years
[d]average over last 3.1 years
[e]average over last 3.5 years

4.7 Properties of the numerical simulations

The simulation chosen for this analysis is the RHD model st35gm03n07 (see Tab. 4.1). This simulation is the closest available to the Betelgeuse effective temperature (3650K, Levesque et al. 2005) and it has the largest number of runs (i.e., it is "relaxed", see Sect. 4.3).
The simulations unveil few large envelope convective cells (the typical structure size is about 400-500 $R_\odot$), evolving on a timescale larger than 3.5 years. In this work, I have analyze in detail the last 3.5 years of the simulation, but I have also checked that the envelope convective cells have a lifetime larger than 7.5 years (i.e., the global period covered for the simulation st35gm03n07, see Sect. 4.3).
Fig. 4.7 and Fig. 4.8 show the temporal evolution of the H band (in the IONIC filter, Fig. 8.4, bottom panel), where the atmosphere is more transparent because we are close to the minimum of H^- opacity. The Figures show the intensity maps that will be analyzed in Chapter 8. In the Figures, the time covered is about 3.5 years and the large structures (400-500 $R_\odot$) don't show radical changes while the intergranular regions and the small (about 50-100 $R_\odot$) dark spots have a lifetime of a few months.
Fig. 4.9 and 4.10 show the averaged velocity computed following Eq. 4.12 at 1.6 μm. The blue color indicates gas approaching the observer while the gas receding is in red. The images show the contribution from different part of the stellar surface to Doppler shifts at that wavelength. I found these pictures really adapted to show the evolution of the large convective cells. In principle, what we can see is pretty similar to the intensity maps in the H band.

The general picture of convection in RHD simulation of red supergiant star is similar to solar-type stars with strong narrow downdrafts (orange-red) surrounded by hot gas that rises slowly (green-light blue) in wide regions (the large central convective cell). Due to the pressure above the granules, the flow is diverted horizontally and a fountain-like topology results. If the pressure is not sufficient to push enough mass out horizontally, the density builds up over the granule. The excess pressure decelerates the upflow.
The light-blue and blue areas, visible on the border of the stellar surface, correspond to the tangential velocities of a flow side on. The flow is growing on the hidden face of the star and it has reached the maximum height in the atmosphere. Its velocities become horizontal. From the observer point of view, these horizontal velocities appear like approaching velocities as sketched in Fig. 4.11.

The large (400-500 $R_\odot$) central granular cell does not change its strong downdraft boundaries within the 3.5 years, even if sometimes they could appear deformed, and it seems that the cell moves to the North-East as shown in Fig. 4.12. There are also small-scale narrow features that develop with red-orange spots or lanes within the large convective cell. These structures divide the granule into fragment and they have a lifetime of few months to one year.
A second cell is visible from the first snapshot (Fig. 4.10) in the left area of the panel: the downdraft redshifted boundaries can be guessed. It becomes more evident only from snapshot 23.038 years (top left panel in Fig. 4.10).
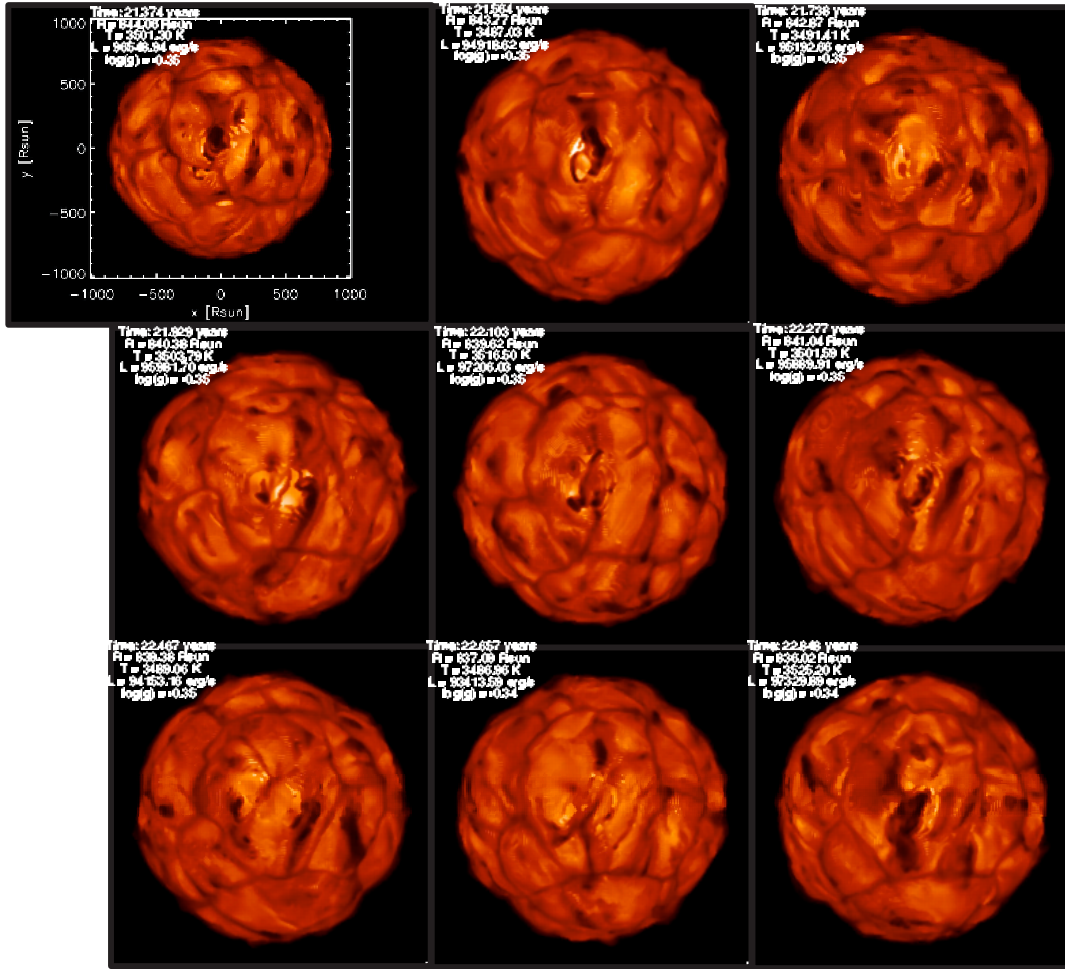
Figure 4.7: Maps of the linear intensity (a scale is used and lighter shades correspond to higher intensities, the range is [0,310000] erg/s/cm^2/Å) in the IONIC filter (see Fig. 8.4, bottom panel). Each panel correspond to a different snapshot of the best model in Tab. 4.1 with a step of about 65 days. The time covered is about 3.5 years. The radius (calculated as described in Sect. 4.3), effective temperature, surface gravity and luminosity are indicated. For the full 3.5 years sequence images with a time-step of about 21 days see Appendix C. The resolution for the calculation is R=50000.

See Appendix D for the complete set of images.

These large convective cells are clearly visible in the stellar "interior" (Sect. 2.3.1) up to temperature of 100000K. In fact, the downdrafts can penetrate down to the model core.
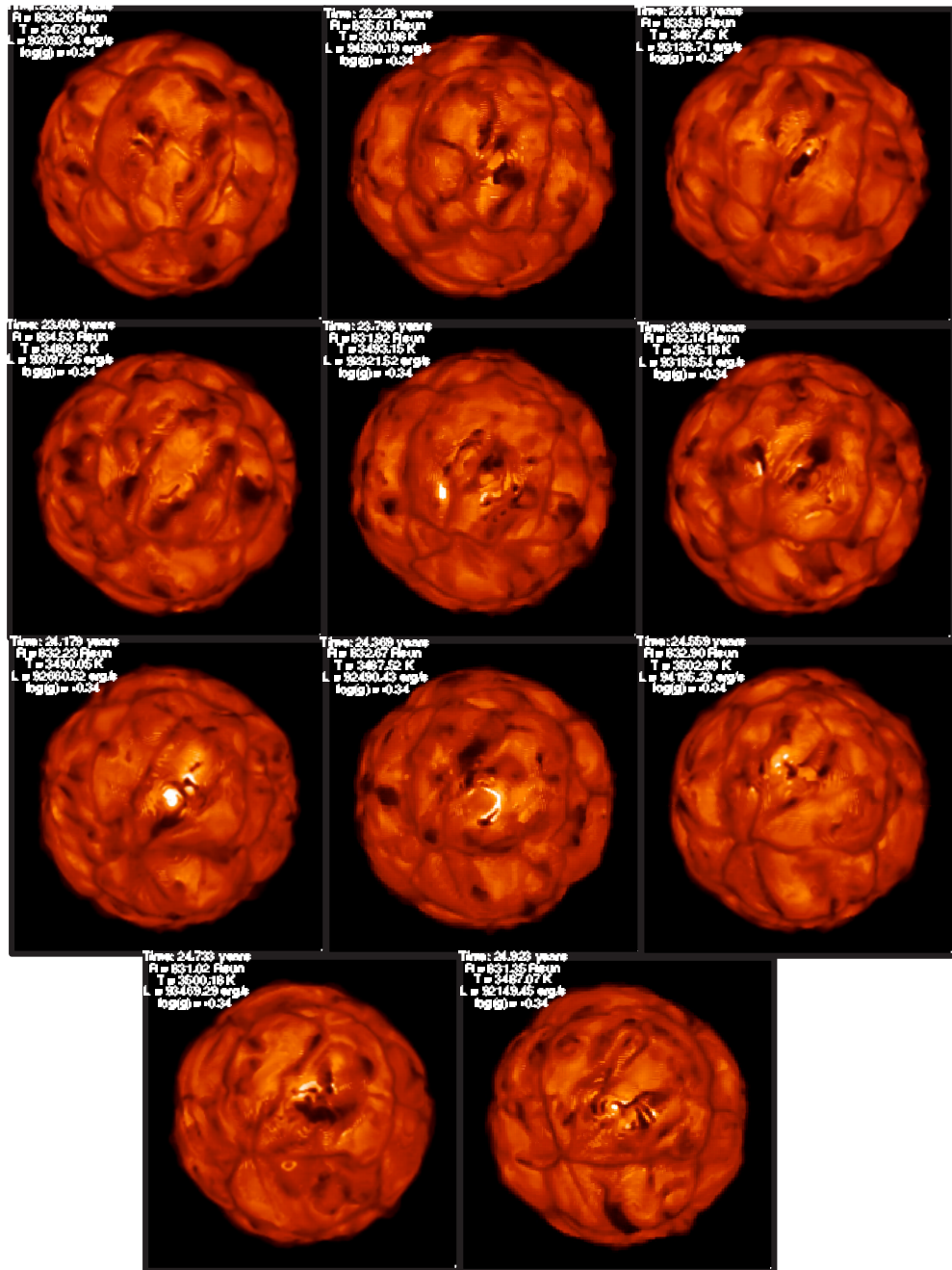
Figure 4.8: Subsequent snapshots (cf. Fig. 4.7).

In order to check if the horizontal size of stellar granules, x_{gran}, can be scaled using stellar parameters, I followed Freytag et al. (1997) who studied this using local models. They found that x_{gran} scales with the pressure scale height at the surface:
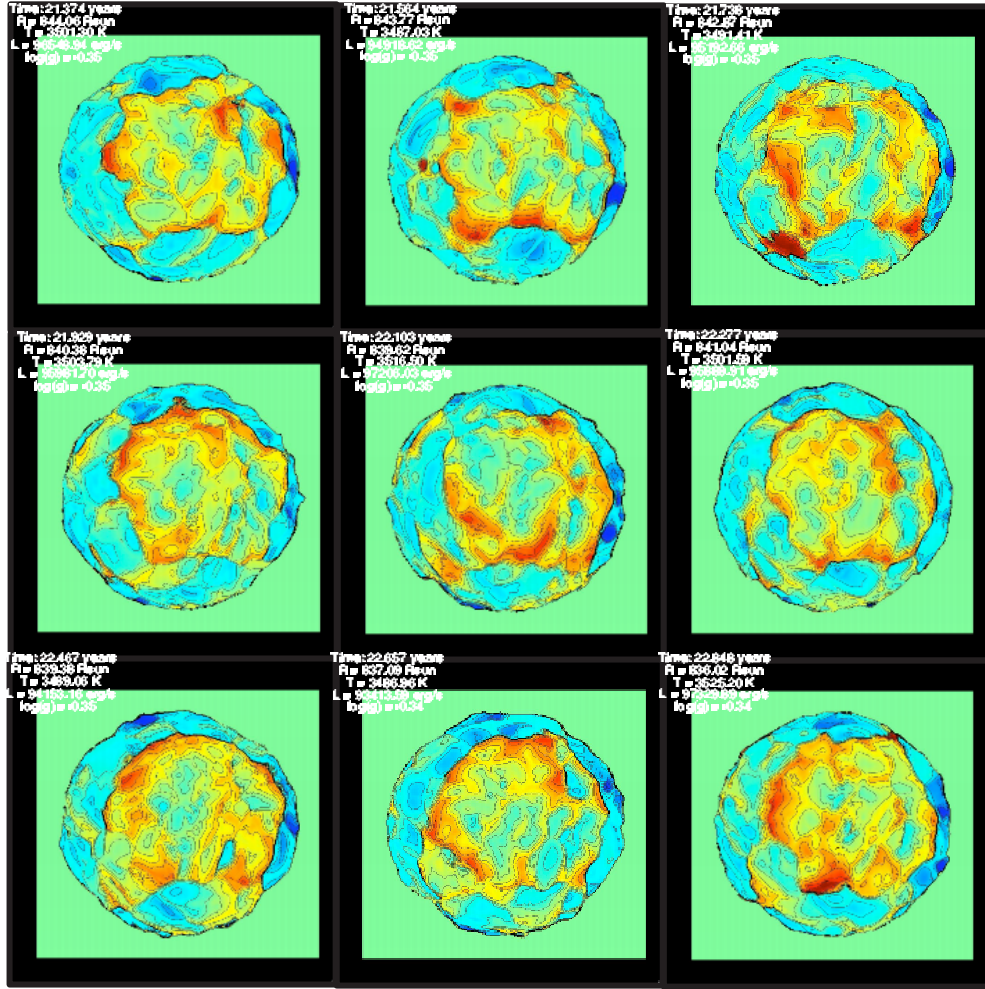
Figure 4.9: Maps averaged velocity computed following Eq. 4.12 at 1.6 μm. Colors follow usual radial convention from red (20 km/s) to blue (-20 km/s), green is zero. The contour black line is the contour plot of the velocity. Each panel correspond to a different snapshot of the best model in Tab. 4.1 with a step of about 65 days. The time covered is about 3.5 years. The radius (calculated as described in Sect. 4.3), effective temperature, surface gravity and luminosity are indicated. For the full 3.5 years sequence images with a time-step of about 21 days see Appendix C.

$$x_{\text{gran}} \approx 10 R \text{T}_{\text{eff}} / g \tag{4.17}$$

where R is the universal gas constant and g the surface gravity. In F2002, this formula is reported as

$$\frac{x_{\text{gran}}}{\text{R}_\star} \approx 0.0025 \times \frac{\text{R}_\star}{\text{R}_\odot} \frac{\text{T}_{\text{eff},\star}}{\text{T}_{\text{eff},\odot}} \frac{\text{M}_\odot}{\text{M}_\star} \tag{4.18}$$
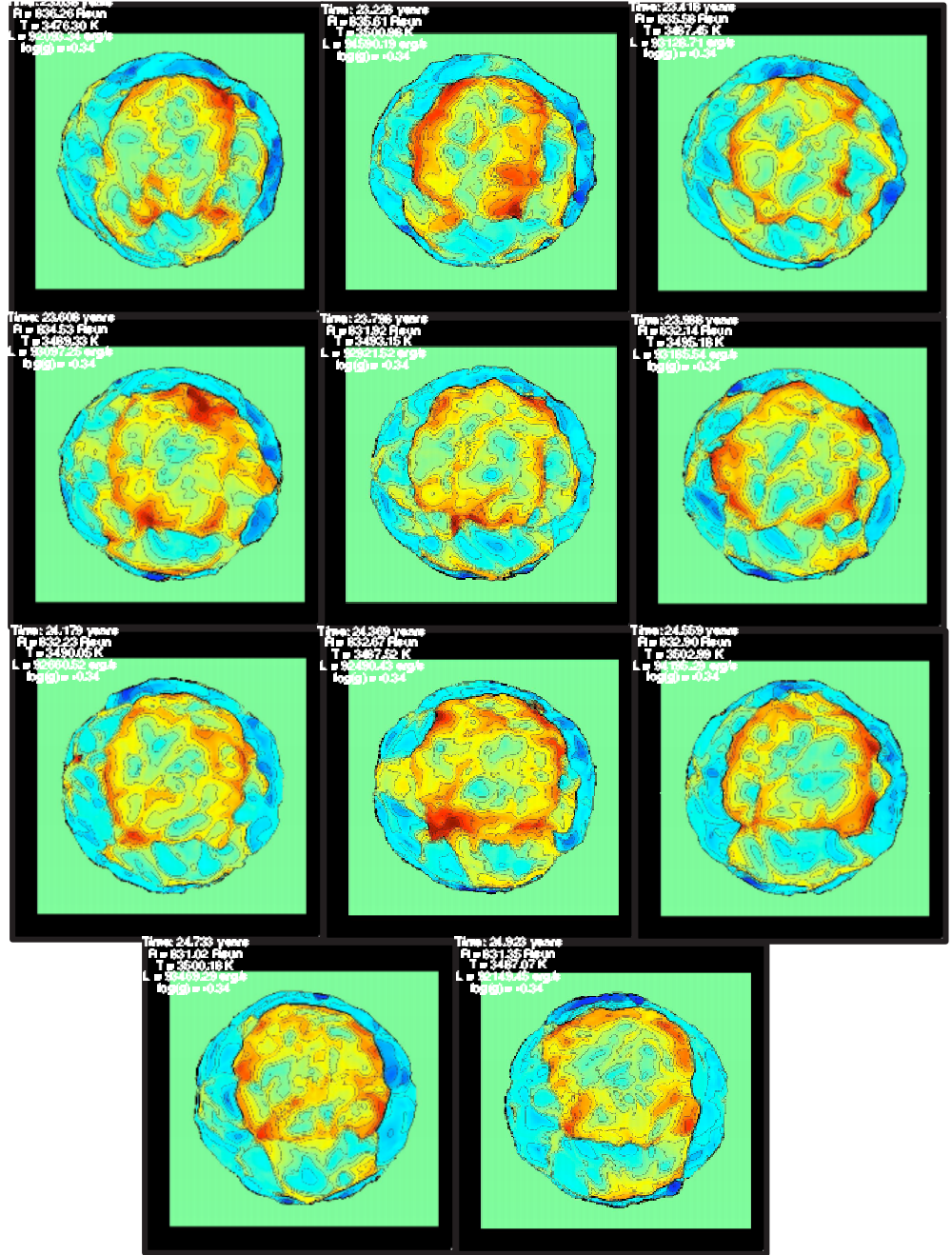
Figure 4.10: Subsequent snapshots (cf. Fig. 4.9).

where $\star$ indicates the stellar parameters and $\odot$ stands for the Sun.
I used in Eq. 4.18 $R_\star$ =836.5 $R_\odot$, $T_{\text{eff},\star}$=3495.2 K and $M_\star$=12 $M_\odot$ (for the model st35gm03n07 in Tab. 4.1) and I obtained $x_{\text{gran}}/R_\star \approx 0.1$. This implies that the entire surface is covered by about 100 convection cells. This could explain the small scale
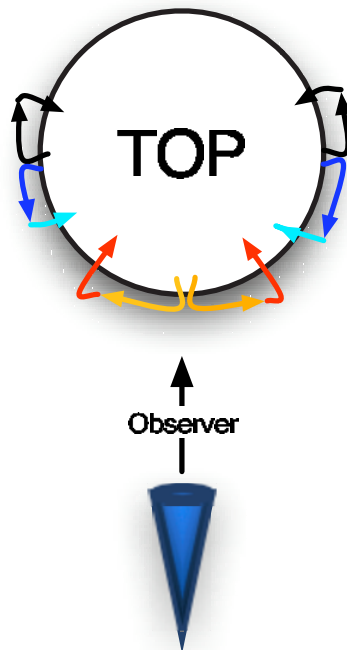
Figure 4.11: Sketch of the flow movements on the surface of the RSG. From the observer point of view, the gas that has reached the maximum height in the atmosphere (yellow orange) stars to plunging on its edges (red). The flows on the other side of the star seem to approach the observer but their velocities are horizontal (blue).

surface structures. What about the large convective cell?

In F2002, there is an explication to the presence of large scale surface structures. Freytag et al. argued that: (i) since the radiative time scales are short, they lead to an efficient damping of small scale temperature fluctuations and favor the formation of large scale structures; (ii) the pressure scale height increase quickly with depth and the deep-penetrating downdrafts probe these layers instead of the surface layers; (iii) finally, the super-adiabatic temperature gradient has high values over a large depth than in the Sun.
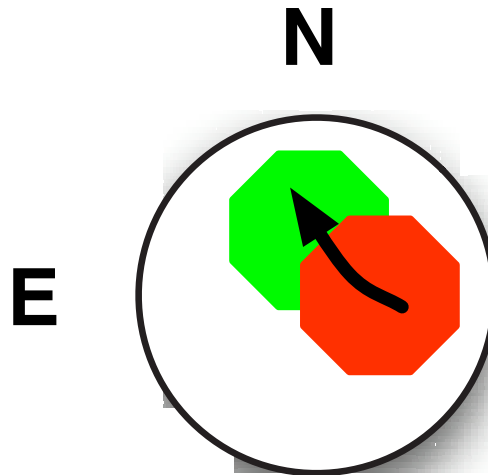
Figure 4.12: Sketch of the qualitatively movement of the central large convective cell visible in Fig. 4.9 and 4.10. The red octagon is approximative position of the cell at 21.374 years, and the green one at 24.923 years. The temporal evolution of the simulation is 3.5 years.

I tried to find a correspondence between the typical lifetime of the convective cells seen in the models and the periods of variability studied by Kiss et al. (2006). Kiss et al. analyzed the light curves collected by the American Association of Variable Star Observers (AAVSO) over the last century. They determine periods of variability from analyses of power density spectra and time-frequency distributions. I report in Tab. 4.2 the period(s) of some bright RSG from Kiss et al. (2006). The dominant large convective elements can explain the observed irregular variations. In fact, while the lifetime of large granules is compatible with long periods, the small-scale structure lifetime is comparable to short periods. Furthermore, the flux of the simulated star in the IONIC filter is reported in Fig. 4.13 as a function of the time (3.5 years covered). Various characteristic features are visible without an apparent regularity. The maximum amplitude is $\sim 5\%$ of the average flux.
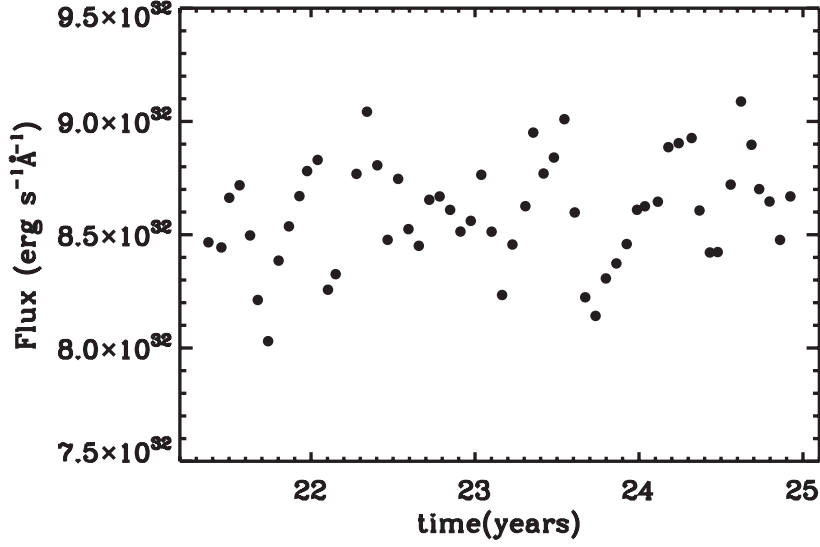
Figure 4.13: Flux of the simulated star at 1.6 μm as a function of the time (3.5 years covered).

Table 4.2: Periods of variability for some observed RSG stars from Kiss et al. (2006)

Star	Period(s)$\pm$ range (years)
α Ori	5.6$\pm$1.3
	1.1$\pm$0.1
μ Cep	2.4$\pm$0.1
	12.0$\pm$2.9
AZ Cyg	1.3$\pm$0.1
	9.2$\pm$3.0
α Her	0.33$\pm$0.01
	1.4$\pm$0.1
	4.0$\pm$0.5
XX Per	8.6$\pm$2.7
α Sco	4.5$\pm$1.7

4.7.1 Properties in other spectral regions

Fig. 4.14 and 4.15 show the intensity maps in the K band (K222-FLUOR filter, see Fig. 8.4, top panel). The convection pattern is similar to what Fig. 4.7 and 4.8 show in the H band. What is different is the surface contrast: the ratio between dark and bright regions is slightly larger in the H band. This has a consequence on interferometric visibility curves and it will be discussed in Sect. 8.4.6.
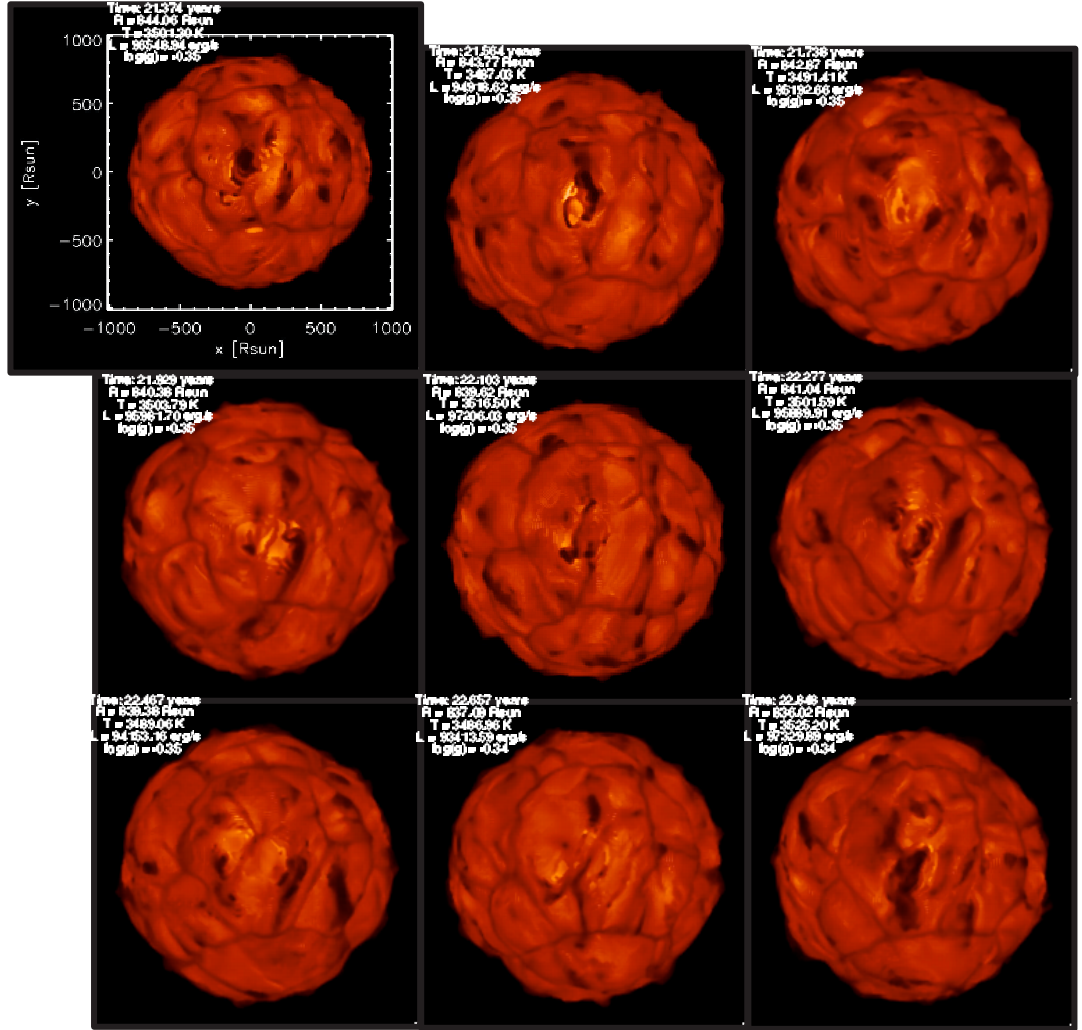
Figure 4.14: Maps of the linear intensity (a temperature scale is used and lighter shades correspond to higher intensities, the range is [0,150000] erg/s/cm^2/Å) in the FLUOR-K222 continuum filter (see Fig. 8.4, bottom panel). Each panel corresponds to a different snapshot of the best model in Tab. 4.1 with a step of about 65 days. The time covered is about 3.5 years. The radius (calculated as described in Sect. 4.3), effective temperature, surface gravity and luminosity are indicated. For the whole images with a time-step of about 21 days see Appendix C. The resolution for the calculation is R=50000.

In the optical, the aspect of the convective pattern changes. Fig. 4.16 compares three different spectral regions in terms of intensity maps and velocity field for one snapshot of the model st35gm03n07 (Tab. 4.1): from the left the intensity map corresponds to the TiO regions between 6100 and 6600Å, then to the K band (K222, Fig. 8.4 top panel) and finally to the H band (IONIC filter, Fig. 8.4 bottom panel). The velocity field is weighted with the contribution function (CF) to the spectral line flux depression (see Sect. 4.1), it is the average velocity of the layers where the line depression is formed.
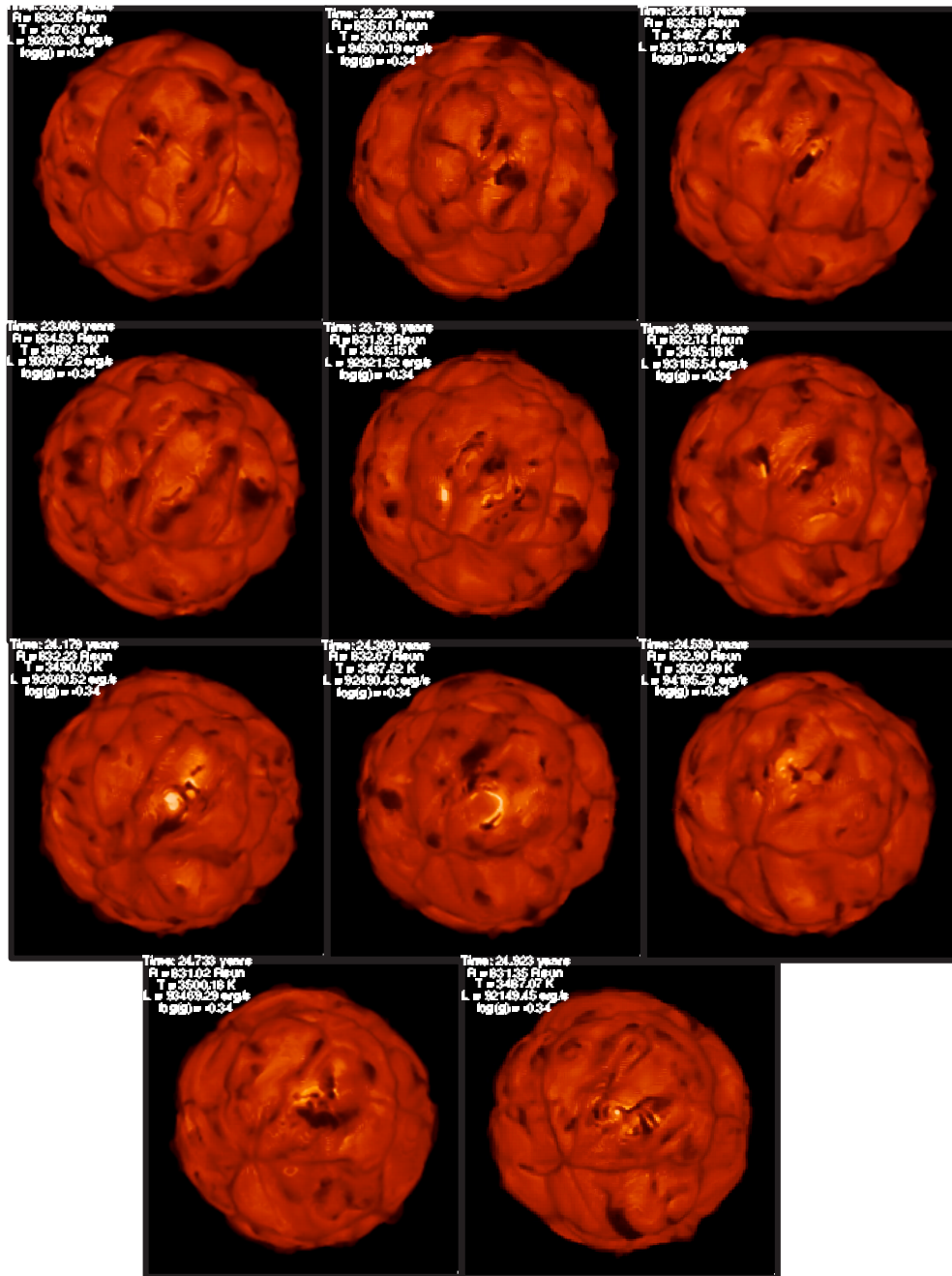
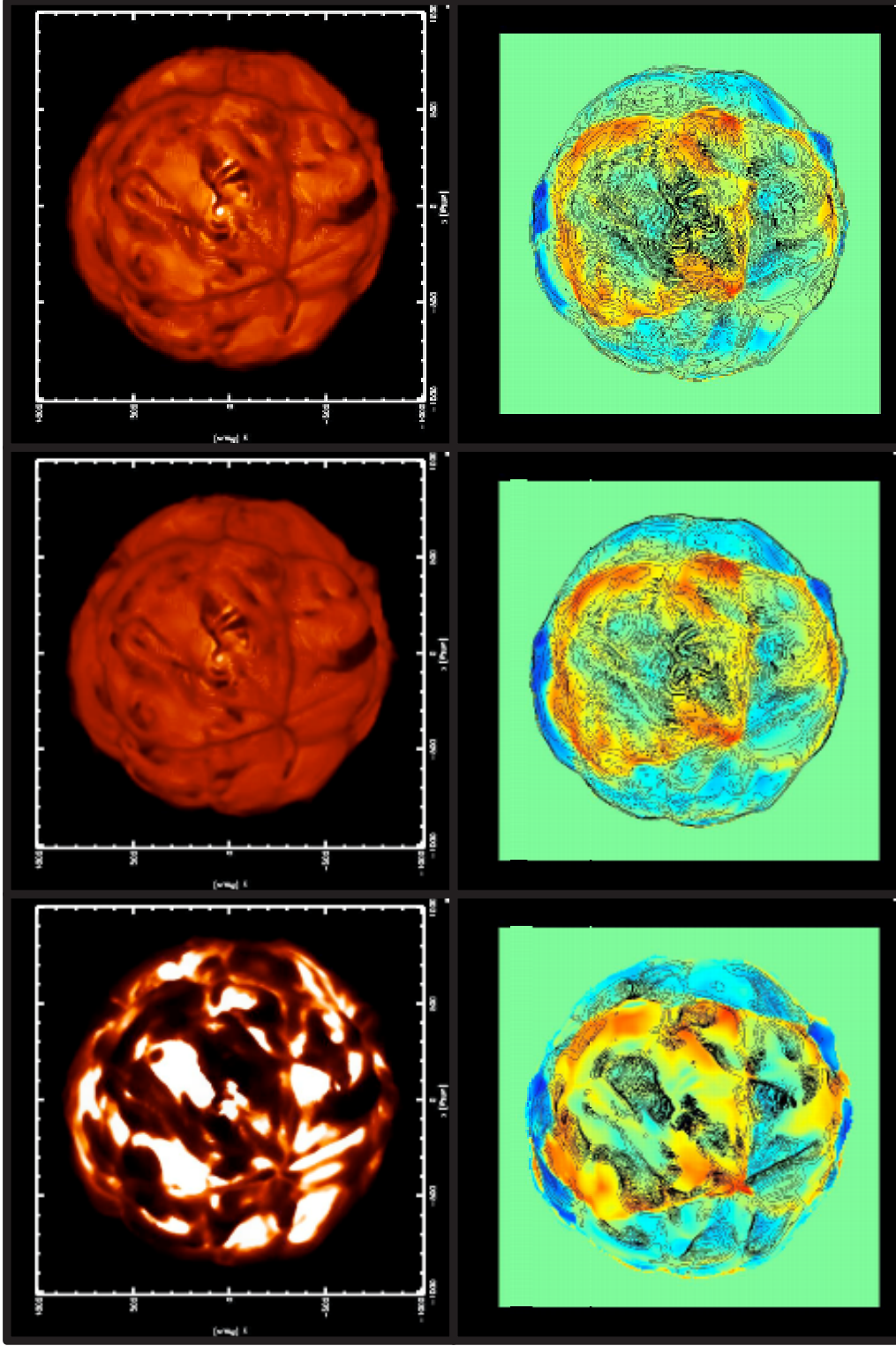**Figure 4.15:** Subsequent snapshots (cf. Fig. 4.14).

Figure 4.16: *Top row:* Maps of the linear intensity for three different spectral regions, from the left the TiO bands between 6100 and 6600Å(intensity range [0,150000] erg/s/cm²Å), then the K band (K222-FLUOR filter - Fig. 8.4 top panel, intensity range [0,150000] erg/s/cm²Å) and the H band (IONIC filter - Fig. 8.4 bottom panel, intensity range [0,310000] erg/s/cm²Å). *Bottom row:* Averaged velocity with the contribution function of the line depression (Sect. 4.1) for the different regions (blue is -20 km/s and red is +20 km/s, green is zero). The contour black line is the intensity.

The intensity maps in the H and K bands (close to the stellar continuum) appear similar: the convective pattern is characterized by bright regions surrounded by dark intersection filaments corresponding to infalling gas. This is confirmed by the velocity field where the convection pattern is evident: the red-green zone in the center corresponds to an upflow that reached the maximum height in the atmosphere and it is plunging on its edge (red). The situation at 6000 Å is quite different. There are not just few distinct big cells on the stellar surface, but hot spots (up to 300000 erg/s/cm²Å) are surrounded by dark patches (few hundreds of erg/s/cm²Å) with complex substructures. The intensity map looks darker (blocking effect, see Sect. 4.4) because the emerging intensity depends on the opacity run through the atmosphere below and TiO veiling is very strong at these wavelengths. As a consequence, there is a contribution of the layers further up in the photosphere where the lines form and the stellar continuum is no longer visible. The star has a radius a bit larger than in the H and K band. In addition, the convection pattern appears different: dark patches cover the large convective cells and the intersection lanes are brighter.

Young et al. (2000) showed an irregular shape of the image of α Ori in the TiO band at 700 nm using parametric models. I have convolved the intensity map in Fig. 4.16 (top left panel) with a rectangular filter in order to have something comparable with the observations. The similitude is striking: in the synthetic convolved image there are two bright spots and possible a third one at the bottom. This comparison qualitatively explains the observation of Young.
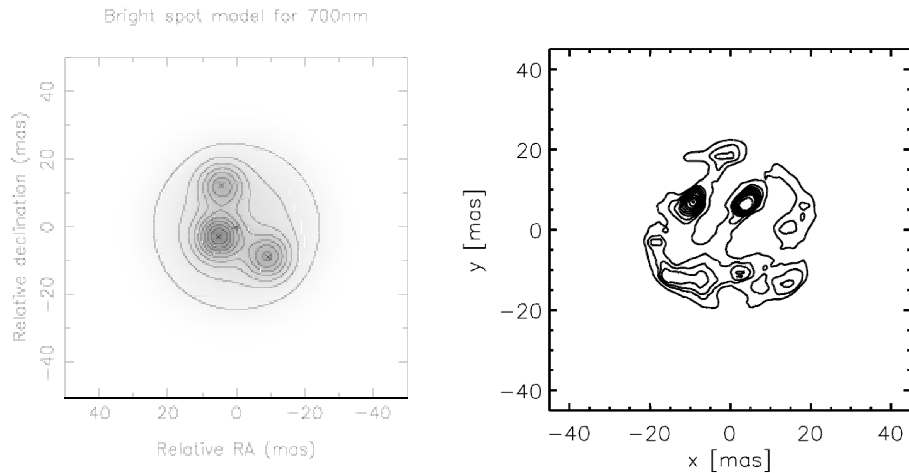

Figure 4.17: *Left panel:* brightness distribution for the best-fitting parametric model with bright feature for α Ori observation (Figure from Young et al. 2000). The brightest areas are shaded darkest. To generate this plot, the features were assumed to be gaussian with FWHM = 10 mas. *Right panel:* contour plot of the brightness distribution obtained from the convolution with a rectangular filter of the image in the TiO band (Fig. 4.16, top left panel). The simulation has been scaled to an apparent diameter of 44.6 mas at a distance of 174.3 pc.

Fig. 4.18 shows three examples of reverse granulation even more striking. The CaI line at 4226.728Å, log(gf)=-0.265 and χ=0. eV (left panel), the CaII H line at 3968.469Å, log(gf)=-0.200 and χ=0. eV (central panel) and the CaII K line at 3933.663Å, log(gf)=0.105 and χ=0. eV (right panel). In the CaI line, the radius of the star is $\sim$ 5% larger than in the H band (Fig. 4.16) and the reverse granulation is clearly distinguishable. In the CaII lines the radius is up to $\sim$ 25% larger than in the H band and shocks outside (i.e., where the gas velocity is larger than the sound velocity of the medium) are remarkable (green circles).

This effect, known as *reversed granulation*, has already been detected in intensity measurements of photospheric spectral lines for the Sun (see for example Janssen & Cauzzi 2006 or Rutten et al. 2004). The reversed granulation is a reversal of the pattern of intensity contrast between intensity maps in the continuum (H and K bands) and intensity maps in spectra lines forming in the middle or upper photosphere (optical region). Cheung et al. (2007) established that this reversal of the intensity fluctuations is a result of the sign change of the horizontal temperature fluctuations, while the velocity pattern remains qualitatively unchanged (see Fig. 4.16). A more detailed investigation on RHD simulation is planned in near future.
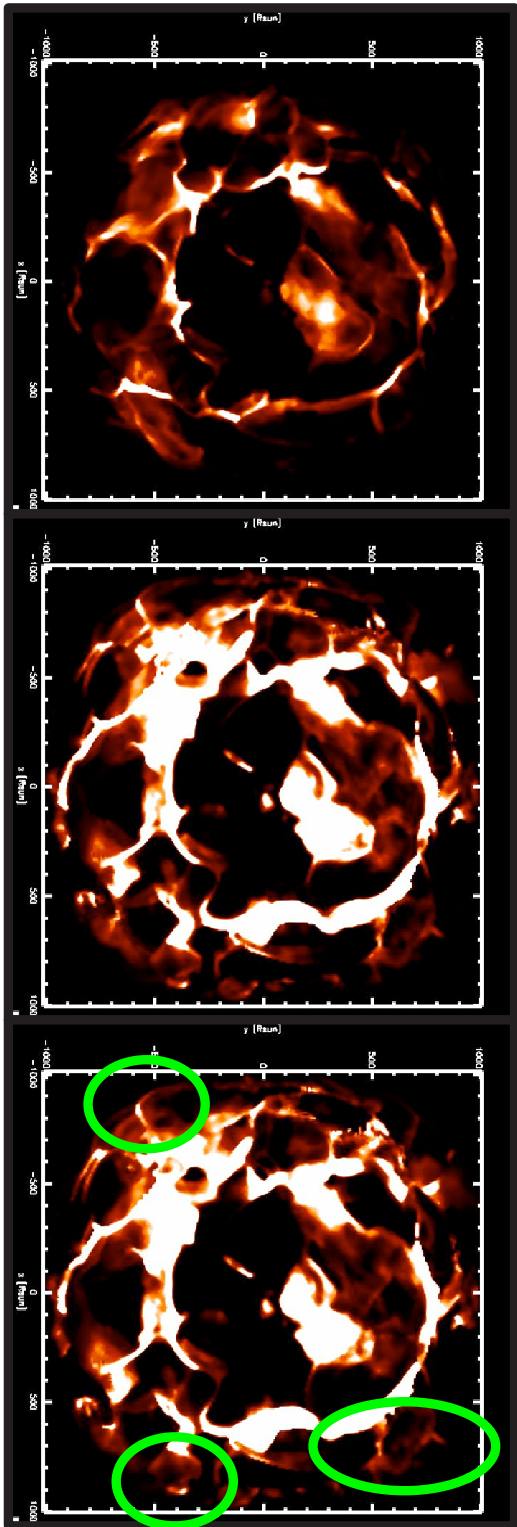
Figure 4.18: Maps of the linear intensity for three different spectral line: CaI line (4226.728Å, log(gf)=-0.265 and χ=0. eV, left panel), the intensity range is [0,10000] erg/s/cm²Å; CaII H line (3968.469Å, log(gf)=-0.200 and χ=0. eV , central panel), the intensity range is [0,2000] erg/s/cm²Å; and CaII K line (3933.663Å, log(gf)=0.105 and χ=0. eV, right panel), the intensity range is [0,2000] erg/s/cm²Å. Green circles indicate shocks. The snapshot of the simulation analyzed is the same as in Fig. 4.16.

4.7.2   Consequence of the convection on the photocenter

The presence of granular flows on the surfaces of RSGs implies ultimate limits to their photometric stability, of the position of their photometric centroid (or photocenter). Interferometric observations with the increasing spatial and spectral resolution of the new generation of telescope will be able to detect the surface brightness distribution (see VSI in Sect. 8.6). Also spectroscopically speaking, the determination of the radial velocities is also connected to the photocenter stability. Stellar micro-variability becomes particularly important for present and future missions such as GAIA and SIM. In this context, granulation-related micro-variability is usually considered as a noise source. The theoretical characterization of granulation micro-variability would help the planning and interpretation of upcoming observations.

In this section I show the displacements of the photocenter introduced by the granulation in the H band (IONIC filter, Fig. 8.4 bottom panel), and in the K band at different wavelengths probing the continuum and CO lines.

Fig. 4.19 shows the temporal fluctuations of the photocenter in IONIC filter (for 3.5 years simulation with a step of $\sim$23 days, left panel) and TiO lines in the TiO electronic transition is the $X^3\Delta$ to $B^3\Pi$ (about 1.5 years covered with a step of $\sim$23 days, right panel). I have used st35gm03n07 simulation in Tab. 4.1. The position of the photocenter is given as the intensity-weighted mean of all light emitting patches tiling the visible stellar surface. In the case of IONIC filter, the photocenter is close to the brightest spot visible close to the stellar center (Fig. 4.7) and there is not a broad movement of the photocenter caused by convection-related dark patches on the surface.

For the TiO band (see the intensity map in Fig. 4.16 to have an idea of the complex surface structures) the photocenter movements are larger and, within the simulated time, the displacement is up to 120 $R_\odot$ ($\sim$ 15% of the stellar radius). If I consider α Ori at 200 pc, this displacement is 2.8 mas!. This is indeed detectable with GAIA and it can be used to calibrate the astrometric measurements.
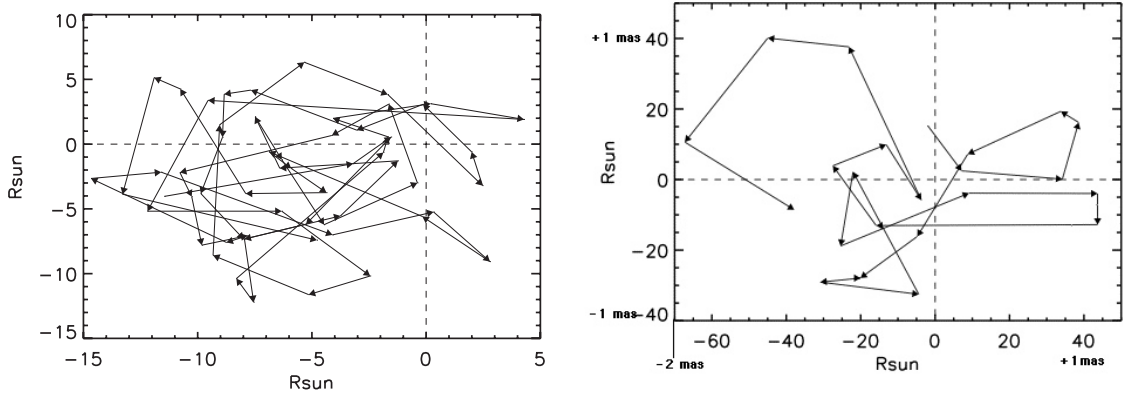
Figure 4.19: *Left panel:* photocenter displacement introduced by the granulation in the H band (IONIC filter). The total time covered is 3.5 years with a time step of about 23 days. The spatial and temporal average radius of the simulation st35gm03n07 is 836.5±4.1 R$_\odot$ (the error is the fluctuations with respect to the average over time, see Tab. 4.1). *Right panel:* photocenter displacement for the TiO electronic transition is the X$^3\Delta$ to B$^3\Pi$ at $\sim$ 6100 Å. The total time covered is 1.5 years with a time step of about 23 days. The indications in milliarcseconds correspond to a star located at 200 pc.

I calculated the intensity maps at the wavelengths of the CO line at 23097.094 Å ($\log(gf)$=-4.195 and χ=1.476 eV, see Sect. 6.2.1) and in the continuum at 2.15 μm with a spectral resolution of 10^5 (CRIRES maximum resolution). The wavelengths probe different depths in the stellar atmosphere. Fig. 4.20 shows that the contrast between large bright granules visible in the continuum (upper-left panel), and the smaller structures seen in the CO line (upper-right panel) is striking. This is due to the convection-related surface structures (see Sect. 8.4.6 and Chiavassa et al. 2008). The position of the photocenter depends on the bright and dark patches on the stellar surface and it varies between the continuum and the CO lines (bottom row). In addition, the photocenter changes positions with time on a time-scale related to the lifetime of the convective structures. The detection of the movement (temporal and spatial) of the photocenter would be a clear signature of the presence of giant convective cells on the surface of RSGs. This is indeed possible with the spectro-astrometric technique (Beckers 1982) with CRIRES (High-Resolution IR Echelle Spectrometer) at VLT. This instrument allows the measure of the two-dimensional position of the photocenter as a function of the wavelength for bright enough stars with a good accuracy (1 mas, J.B. Le Bouquin private communication; this corresponds to the movement of the photocenter visible in Fig. 4.19 about 20 R$_\odot$ for a RSG a 200 pc is $\sim$1 mas).

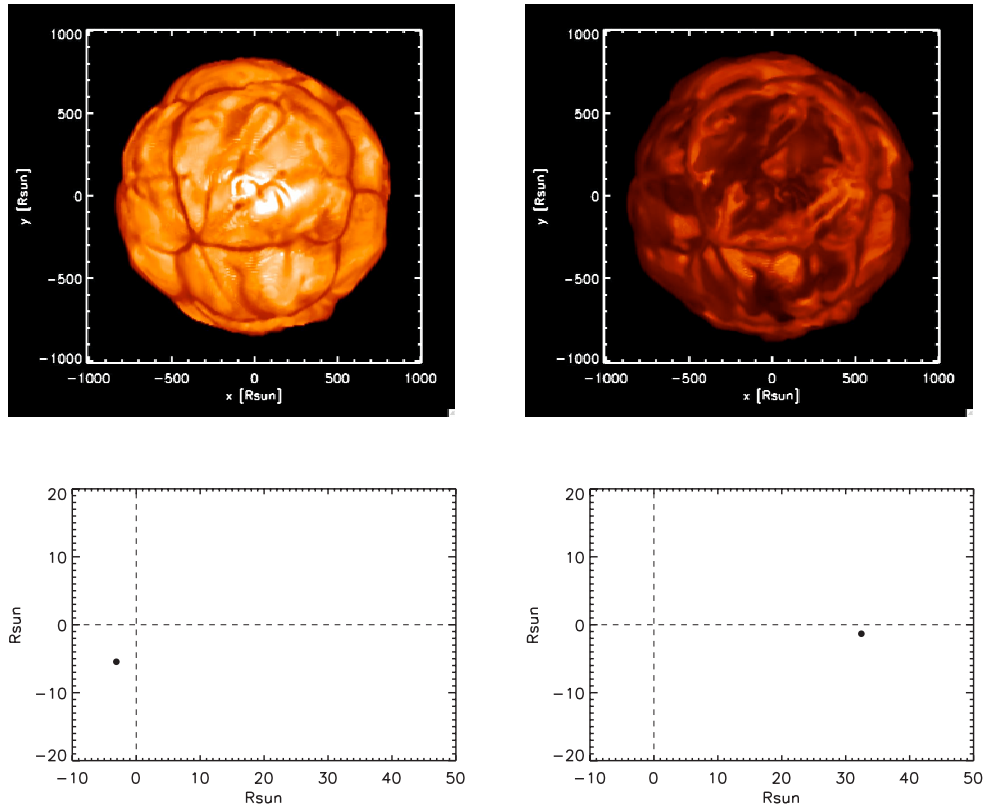**Figure 4.20:** Maps of the linear intensity (top frames, the intensity range is [0,90000] erg/s/cm^2/Å) at different wavelengths and photocenter positions (bottom frames). *Left column:* continuum at 21500±0.1104Å(spectral resolution of 10000A). *Right column:* CO line at 23097±0.1104Å(spectral resolution of 10000A). The resolution for the calculation is R=500000.

4.8   Velocity fields

The characterization of the velocity fields in RHD simulations is a very important task to achieve the comprehension of the observed spectral asymmetries and shifts.
Fig. 4.22 reports the radial velocity (top panel) and the velocity (bottom panel) of the RHD simulation st35gm03n07.
The radial velocity is defined as $\langle v|r \rangle$ where $\vec{v} = \sqrt{v_{x1}^2 + v_{x2}^2 + v_{x3}^2}$ and
$\vec{r} = \sqrt{x1^2 + x2^2 + x3^2}$. Just below the photosphere at 800 R$\odot$, high negative (i.e., gas approaching the observer) velocities and, in the stellar interior at 650 R$\odot$, positive (i.e., gas moving inwards) velocities are a consequence of the strong convective motions. As already mentioned in Sect. 2.3.3 the shock peak velocities saturates near values of about 25 km/s, nearby the sound speed drop. Close to the surface, the Mach number of the convective flow (Fig. 4.21) becomes larger, and in the upper photosphere the flow is typically supersonic.
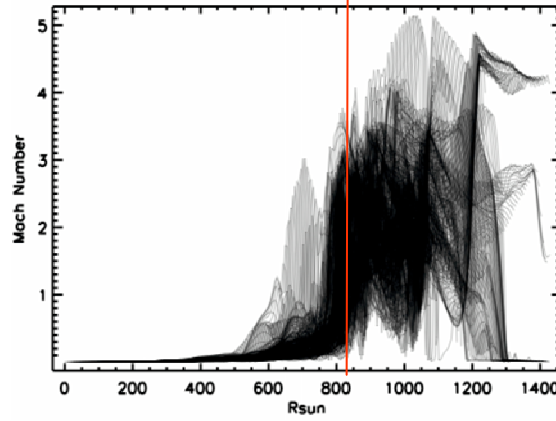

Figure 4.21: Typical Mach numbers of a snapshot of the relaxed simulation st35gm03n07. The red line indicates the radius.
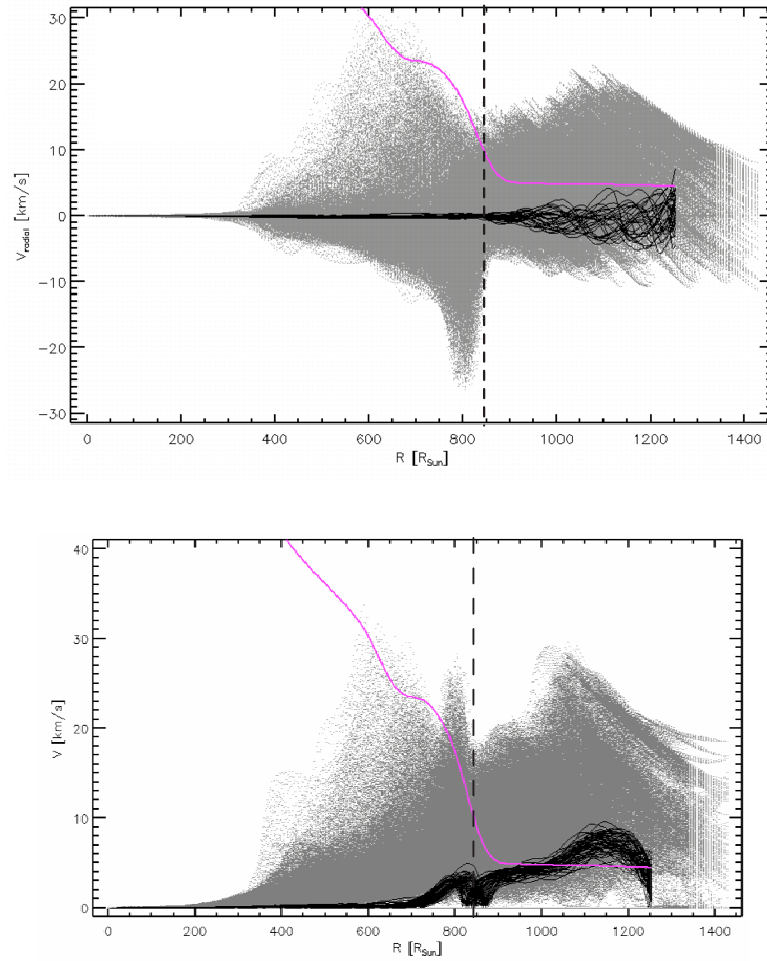
Figure 4.22: Velocity in RHD models (st35gm03n07) within 3.5 years of simulations. *Top panel:* Radial velocity (grey) for all the positions in the cube. Radial velocity average over spherical shells (black). Sound speed (purple). *Bottom panel:* velocity (grey) for all the positions in the cube and for a temporal evolution. Velocity average over spherical shells (black). Dashed line shows the approximative location of the stellar radius. Sound speed (purple).